

Enhancing resonant circular-section haloscopes for dark matter axion detection: approaches and limitations in volume expansion

J.M. García-Barceló,^{*,a} A. Díaz-Morcillo,^b B. Gimeno^c

^a*Max-Planck-Institut für Physik (Werner-Heisenberg-Institut), Föhringer Ring 6, 80805 München, Germany*

^b*Department of Information Technologies and Communications, Universidad Politécnica de Cartagena, 30203 - Cartagena, Spain*

^c*Instituto de Física Corpuscular (IFIC), CSIC-University of Valencia, 46980 - Valencia, Spain*

**Corresponding author*

E-mail: jmgarcia@mpp.mpg.de

ABSTRACT: Haloscopes, microwave resonant cavities utilized in detecting dark matter axions within powerful static magnetic fields, are pivotal in modern astrophysical research. This paper delves into the realm of cylindrical geometries, investigating techniques to augment volume and enhance compatibility with dipole or solenoid magnets. The study explores volume constraints in two categories of haloscope designs: those reliant on single cavities and those employing multicavities. In both categories, strategies to increase the expanse of elongated structures are elucidated. For multicavities, the optimization of space within magnets is explored through 1D configurations. Three subcavity stacking approaches are investigated, while the foray into 2D and 3D geometries lays the groundwork for future topological developments. The results underscore the efficacy of these methods, revealing substantial room for progress in cylindrical haloscope design. Notably, an elongated single cavity design attains a three-order magnitude increase in volume compared to a WC-109 standard waveguide-based single cavity. Diverse prototypes featuring single cavities, 1D, 2D, and 3D multicavities highlight the feasibility of leveraging these geometries to magnify the volume of tangible haloscope implementations.

Contents

1	Introduction	1
2	Single cavities	7
2.1	Long cavities	7
2.2	Tuning	11
3	1D multicavities	12
3.1	Stacking in φ	12
3.2	Stacking in ρ	15
3.3	Stacking in length	17
3.4	Possibilities for increasing the subcavity volume	17
3.4.1	Long subcavities	19
3.4.2	Large diameter subcavities	20
3.5	Tuning	21
4	2D and 3D multicavities	22
4.1	Stacking in φ and ρ	22
4.2	Stacking in φ and length	23
4.3	Stacking in ρ and length	24
4.4	Stacking in φ , ρ , and length	25
4.5	Hexagonal multicavities	26
4.6	Tuning	28
5	Conclusions and prospects	28

1 Introduction

In recent decades, there has been a lot of interest in axions and other particles compatible with the Standard Model that could be part of dark matter. Axions, the particles proposed by Weinberg [1] and Wilczek [2], might address the strong Charge Conjugation-Parity problem [3, 4]. A few years later, utilising the misalignment hypothesis, it was projected that axions may perhaps constitute dark matter [5–7].

Several research groups have constructed during the last thirty years experimental devices to look for axions, which are based on the inverse Primakoff effect [8, 9]. These detection methods are further classified into three varieties based on the origin of the axion source: haloscopes, helioscopes, and Light Shining through Walls (LSW). The last one produces axion particles intentionally in the laboratory. However, haloscopes and helioscopes

rely on external natural sources (relic axions from the galactic halo or axions from the Sun, respectively). They are all based on the axion-photon conversion, which is boosted by an external magnet with a high level of magnetostatic field. Furthermore, in the case of haloscopes, this conversion can be enhanced by using high-quality factor resonators (such as microwave cavities).

At present, the forefront of experiments aimed at detecting axions is centered on the haloscope framework, remarkably exemplified by the ADMX (Axion Dark Matter eXperiment) [10] and CAPP (Center for Axion and Precision Physics) [11] initiatives. These groups operate below 1 GHz and above 1 GHz frequency domains, respectively. In the helioscope scenario, the CAST (CERN Axion Solar Telescope) investigation [12], albeit decommissioned, and the forthcoming IAXO (International Axion Observatory) [13] project assume fundamental roles.

In anticipation of IAXO, the BabyIA XO magnet prototype emerges as a first prototype, affording a versatile platform for both helioscope and haloscope axion experiments [14]. The high-volume magnetic configurations featured in the IAXO and BabyIA XO magnets not only demonstrate cost-effectiveness at low frequencies [15] but also facilitate the establishment of haloscopes with large volumes operating at higher frequencies [16]. These experimental efforts are actively working to achieve sensitivities aligned with the KSVZ (Kim-Shifman-Vainshtein-Zakharov) and DFSZ (Dine-Fischler-Srednicki-Zhitnitsky) models, which offer promising potential for detecting axions [14].

Remarkably, the ADMX collaboration has achieved significant sensitivities within the $2.81 - 3.31 \mu\text{eV}$ range [17]. Noteworthy is the recent proposition by the CAPP consortium, outlining an axion dark matter exploration through a DFSZ-sensitive haloscope spanning the 4.51 to $4.59 \mu\text{eV}$ axion mass range [11]. Furthermore, the HAYSTAC (Haloscope At Yale Sensitive To Axion Cold Dark Matter) group has achieved KSVZ-sensitive outcomes from dual independent searches for dark matter axions within the 16.96 to $17.28 \mu\text{eV}$ and 23.15 to $24.0 \mu\text{eV}$ axion mass intervals [18, 19]. Clearly, these experimental teams are making progress in achieving sensitivities that hold significant theoretical importance within the realm of haloscope investigations.

Beyond the aforementioned initiatives, other axion groups like RADES [20], QUAX [21], and FLASH [22, 23] have also made noticeable progress in enhancing the utilization of haloscope methodologies in recent times.

The whole setup of the haloscope involves a mix of essential parts. First of all, a suitable cavity designed to operate at the frequency where the axion search will take place is required. On the other hand, due to the extremely weak interaction between axions and photons, it's crucial to maintain a cryogenic environment at temperatures in the Kelvin range. This helps minimize any unwanted heat effects. In addition, for boosting the axion-photon conversion, a high static magnetic field is needed. Thus, a magnet is necessary,

where the resonant cavity will be installed. After that, the radio frequency (RF) power collected within the haloscope goes through a series of changes including amplification, filtering, and down-conversion, culminating in its interception by a receiver.

At the final stage, the receiver steps in to handle main operations, including converting analog signals into digital format. This is followed by a process of data manipulation, achieved using Fast Fourier Transform algorithms, a standard technique widely implemented in the theory of signal processing [20].

A fundamental objective inherent in the design of an axion detection configuration revolves around the augmentation of the axion-photon conversion sensitivity in the haloscope device. This increase, which depends on a specific signal-to-noise ratio ($\frac{S}{N}$), can be easily formulated through [24]

$$g_{a\gamma} = \left(\frac{\frac{S}{N} k_B T_{sys} (1 + \beta)^2}{\rho_a C V \beta Q_0} \right)^{\frac{1}{2}} \frac{1}{B_e} \left(\frac{m_a^3}{Q_a \Delta t} \right)^{\frac{1}{4}}, \text{ provided that } Q_a \gg \frac{Q_0}{1 + \beta} \quad (1.1)$$

where $\frac{S}{N}$ is the signal-to-noise ratio, k_B is the Boltzmann constant, T_{sys} is the noise temperature of the system expressed in K, β is the extraction coupling factor, ρ_a is the dark matter volumetric density, C is the form factor of the cavity mode, V is the volume of the haloscope, Q_0 is the unloaded quality factor, B_e is the maximum intensity of the external magnetostatic field \vec{B}_e , m_a is the axion mass (directly proportional to the operational frequency of the experiment), Q_a is the axion quality factor, and Δt is the time window used in the axion data campaign. A requisite condition for achieving optimal power transfer is the attainment of a β value equal to unity ($\beta = 1$), the so-named critical coupling regime. It is crucial to emphasize that the properties of the external static magnetic field (\vec{B}_e) depend on the particular magnet arrangement utilized in the experimental setup, typically being of either solenoidal or dipolar type. Furthermore, the spatial distribution and polarization of this magnetic field need to be analysed carefully since they play a key role in selecting the operation mode (axion mode) in the resonant device.

Despite its pronounced high-Q resonant characteristics, the ultimate objective of a cavity-based haloscope is the exploration of a wide range of mass values accomplished in a time-efficient manner. The process of mass variation encompassing a breadth of values is facilitated through the integration of efficient mechanical mechanisms or the strategic deployment of materials capable of shifting the resonant frequency of the cavity. The quantification of the rate at which this mass exploration runs is denoted as the scanning rate, often employed as a key parameter encapsulating the efficacy and performance of the haloscope.

In the context of conducting a measurement wherein the resonance of the cavity is aligned with the axion mass m_a , considering the temporal requisites for effecting achieve a

predetermined level of $\frac{S}{N}$, the scanning rate can be expressed as [24]

$$\frac{dm_a}{dt} = Q_a Q_0 \frac{\beta^2}{(1 + \beta)^3} g_{a\gamma}^4 \left(\frac{\rho_a}{m_a} \right)^2 B_e^4 C^2 V^2 \left(\frac{S}{N} k_B T_{sys} \right)^{-2}. \quad (1.2)$$

The form factor serves as a parameter that gives the parallelism between the external static magnetic field (\vec{B}_e) and the radio frequency electric field (\vec{E}), the latter being induced within the cavity through the axion-photon interaction. This key indicator is mathematically characterized as follows:

$$C = \frac{|\int_V \vec{E} \cdot \vec{B}_e dV|^2}{\int_V |\vec{B}_e|^2 dV \int_V \varepsilon_r |\vec{E}|^2 dV}. \quad (1.3)$$

In this equation, the symbol ε_r stands representative of the relative electric permittivity present in the cavity medium, which predominantly comprises air or vacuum. Thus, the modifiable and optimizable facets within the design of a haloscope resonator encompass this set of parameters: β , C , V , and Q_0 . In this work, in order to measure the performance of the cavity structure, we will use $Q_0 V^2 C^2$, following 1.2.

The principal objective of this investigation revolves around an analysis for amplifying the volumetric dimensions of haloscopes employing cylindrical structures. As a result of this expansion, enhanced sensitivity and scanning rate for the detection of axions are envisaged. Noteworthy precedent explorations pertaining to the viability of rectangular cavities were previously conducted and discussed in [16]. In the present article, a similar study is intended to be carried out for haloscopes with a circular cross-section, which is more common in dark matter axion experiments, since it makes better use of the volume of the cylindrical bores of the magnets. For a haloscope design, the maximum admissible volume is essentially determined by four key factors that interact together: the geometry of the cavity, the specific electromagnetic mode and the operational frequency employed, the use of multicavity approaches, and the magnet system's geometry and typology (how exactly the magnetic field is aligned for measuring axions).

The characteristic resonant frequency associated with cylindrical cavities engaged in TE_{mnp} and TM_{mnp} modes can be expressed as follows:

$$f_{TE_{mnp}} = \frac{c}{2\pi \sqrt{\varepsilon_r \mu_r}} \sqrt{\left(\frac{\chi'_{mn}}{a} \right)^2 + \left(\frac{p\pi}{d} \right)^2}, \quad \begin{array}{l} m = 0, 1, 2, \dots \\ n = 1, 2, 3, \dots \\ p = 1, 2, 3, \dots \end{array} \quad (1.4)$$

$$f_{TM_{mnp}} = \frac{c}{2\pi \sqrt{\varepsilon_r \mu_r}} \sqrt{\left(\frac{\chi_{mn}}{a} \right)^2 + \left(\frac{p\pi}{d} \right)^2}, \quad \begin{array}{l} m = 0, 1, 2, \dots \\ n = 1, 2, 3, \dots \\ p = 0, 1, 2, \dots \end{array} \quad (1.5)$$

where c is the speed of light in vacuum; μ_r is the relative magnetic permeability ($\mu_r = \varepsilon_r = 1$ is imposed in this paper); m , n , and p are integers that denote the number of maxima of the

electric field magnitude along the φ (azimuth), ρ (radius), and z (length) axes, respectively; χ_{mn} and χ'_{mn} are the n -th zeros of the Bessel function J_m and its derivative J'_m of order m , respectively; and a and d are the radii and length of the cavity, respectively. As highlighted by the equation provided, the frequencies at which resonance occurs depend on the size of the cavity. This mathematical connection shows the difficulties of trying to increase the volume of the cavity and the operational frequency at the same time. In addition, the mode clustering should be avoided, which could introduce higher complexity in the cavity design pointing out the potential challenges in achieving these two goals simultaneously.

The challenge of mode clustering, dictating the interaction between the principal mode and its subsequent higher order counterparts, can result in a diminution in the form factor parameter of the desired mode. This issue persists even when higher order modes manifest form factors attaining a null value.

Solenoids, as depicted in Figure 1a, constitute the predominant selection of magnets deployed within experimental frameworks for the detection of dark matter axions. These

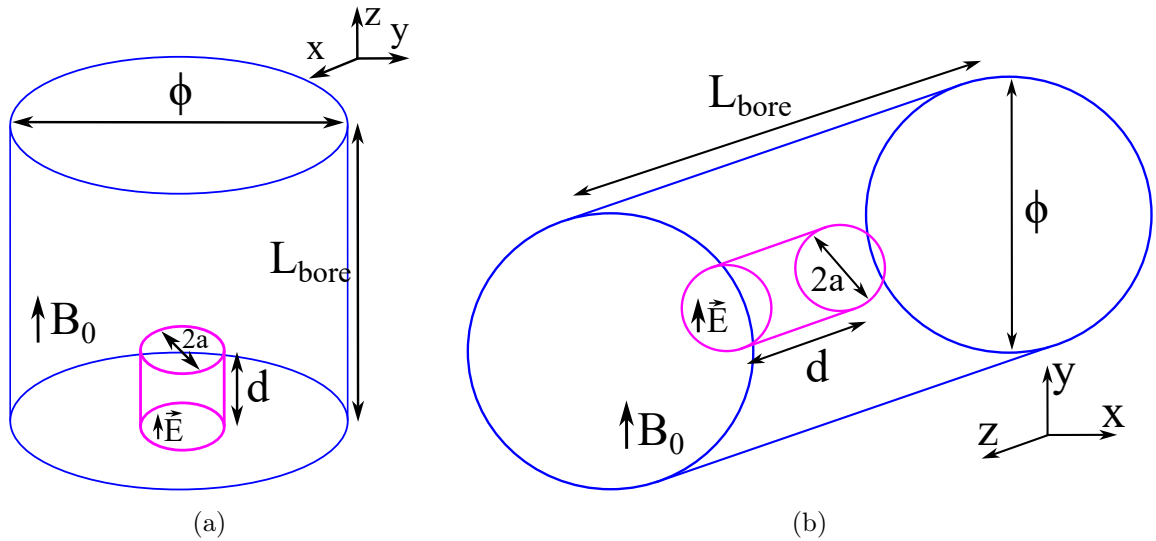


Figure 1: (a) Solenoid magnet (blue) featuring a cylindrical cavity (pink) characterized by a radius a and a length d , designed to operate within the ambit of the TM_{010} cylindrical mode, and (b) dipole magnet (blue) housing a similar cavity (pink) but now working with the TE_{111} cylindrical mode. Notably, for the solenoid magnet, the predominant orientation of the magnetic field primarily aligns with the z -axis, whereas for the dipole magnet this alignment is predominantly directed along the y -axis. It is crucial to remark that although the illustration does not overtly indicate, it is assumed that the probes designated for external couplings shall be situated along the upper boundaries of the cavities, aligning with the z -axis in (a) and the y -axis in (b).

solenoidal magnets have a specialized role in important research projects, as demonstrated by their use in notable initiatives like ADMX [17], CAPP [11], and HAYSTAC [25]. The

axial (z -axis) static magnetic field they generate is aligned with the electric field of the TM_{010} cylindrical mode, contributing to an optimal form factor. In contrast, accelerator dipole magnets (see Figure 1b), as the CAST magnet, give a robust transverse static magnetic field, which necessitates the employment of a cylindrical cavity operating under the TE_{111} mode. This setup mainly leads to vertical polarization, where the RF electric field aligns mostly parallel to the static magnetic field in the dipole arrangement [15, 26].

Furthermore, an illustrative example worth considering is the future BabyIAXO experiment, which deploys a superconducting toroidal magnet, and its magnetic field pattern is presented in [14]. Nevertheless, for the purpose of this paper, the BabyIAXO configuration can be conveniently treated as akin to a dipole magnet. It is pertinent to note that in this study, for the purpose of calculating the form factor, a simplified approximation implies the assumption of a uniform static magnetic field $\vec{B}_e = B_e \hat{y}$ for the dipole and quasi-dipole magnet (i.e. BabyIAXO) configurations [14].

A comprehensive overview encompassing the most commonly utilized magnets by several research groups is shown in [16]. For a clarification of the optimal alignment of cylindrical cavities with solenoid and dipole magnets, refer to Figure 1.

As a general trend, the aspect ratio characterizing the bore of dipole magnets leads towards a considerably large configuration relative to their diameter. Conversely, the bores of solenoid magnets usually have dimensions where the length and diameter look more alike. Consequently, the main objective for increasing the volume in the haloscope involves calibrating the cavity geometry to effectively exploit the available room within the magnet bore. One of the pioneering efforts that aimed to make the most of elongated cavities was seen in the development and execution of a toroidal-shaped cavity, an initiative from the CAPP team [27, 28]. Notably, in this scenario, the BabyIAXO magnet steps up as a perfect fit for this pursuit. Nonetheless, it's worth noting the rise of novel geometries as potential paths to explore, like incorporating large structures in rectangular setups, which presents an attractive idea [16].

It is important to point out here other interesting concepts for obtain high frequencies-high volumes, not related to multicavities, as wire array [29] or dielectric array [30] meta-material cavities, or phase-matched multiple cavities [26].

In Section 2, we expose the thorough investigations conducted aiming to uncover the limitations of volumetric capacities in haloscopes for long single cylindrical cavities operating with TM_{010} and TE_{111} modes. The central objective is to establish these critical thresholds, and a meticulous analysis is dedicated to scrutinizing frequency spacing (mode clustering) examining the form factor, quality factor and volume parameters for the optimization of axion detection.

Following this, Section 3 introduces a new concept: one-dimensional (1D) multicavity

configurations based on cylindrical subcavities interconnected via iris windows. Three spatial orientations are analysed for the couplings between subcavities: φ , ρ , and z axes. In addition, two scenarios are explored in these haloscopes: dipole and solenoid configurations, considering the magnets presented in [16]. To see how these new setups measure up against standard single cavities, a detailed comparison by examples that work in the X-band frequency range (8 – 12 GHz) is shown, analysing the key cavity parameters (form factor, quality factor, and volume). Furthermore, this paper systematically clarifies approaches aimed at enhancing the volume of cylindrical subcavities, encompassing both length and diameter.

Section 4 establishes a framework based on the expansion of the multicavity concept into the realms of two-dimensional (2D) and three-dimensional (3D) structures. In this study, the combination of different stacking orientations for the coupling between subcavities is explored. The discussion introduces various illustrative examples of 2D and 3D multicavity arrangements. These instances serve as effective means to clarify the benefits provided by these evolved structures when compared to their one-dimensional (1D) counterparts highlighting its potential in optimizing the efficient utilization of magnets for axion search experiments.

Finally, Section 5 shows the conclusions of the present investigations detailing future lines of work arising from these studies.

2 Single cavities

The TM_{010} mode is used for cylindrical cavities operating in solenoid magnets because it maximises the form factor stated in equation 1.3. Because the length of the cavity d has no effect on the resonant frequency in this mode, it can be adjusted as desired to expand the cavity volume. However, there is a limit where d cannot be raised owing to the proximity of higher order modes with $p \neq 0$ (in this case, the nearest mode is the TM_{011}). This scenario may impede accurate mode identification and, in some situations, may lower the form factor.

On the other hand, in dipole magnets the TE_{111} is usually employed working with cylindrical cavities. The simplest way to raise the length of the haloscope without decreasing the resonant frequency is to slightly reduce the radius a , according to equation 1.4. Because this reduction is little in comparison to the length gained, the overall volume will be increased. Furthermore, when the cavity length is substantially greater than its radius, the resonant frequency becomes virtually independent of the cavity length ($f_{TE_{111}} \approx \frac{c\chi'_{11}}{2\pi a}$). Again, the restriction is enforced by the closeness of the next resonant mode (in this case, with the TE_{112} mode).

2.1 Long cavities

Figure 2 shows the relative mode separation Δf for a cylindrical cavity as a function of d/a for both scenarios, solenoid and dipole.

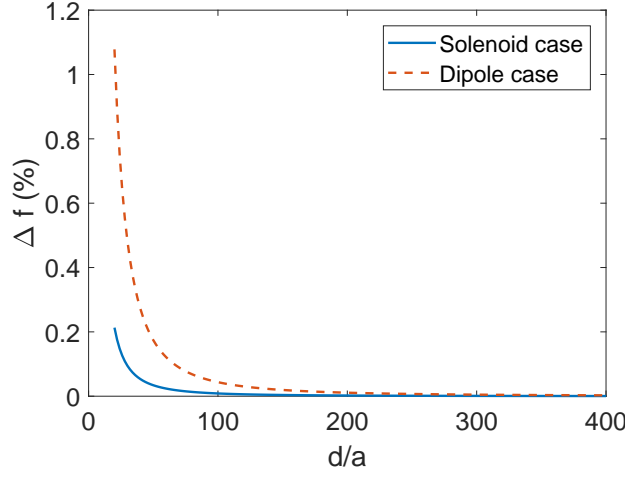


Figure 2: Relative mode separation between modes TM_{010} and TM_{011} (solenoid case) (blue solid curve) and between modes TE_{111} and TE_{112} (dipole case) (red dashed curve) versus d/a .

This mode separation is defined as

$$\Delta f = \frac{|f_{axion} - f_{neighbour}|}{f_{axion}} \times 100 \quad [\%] \quad (2.1)$$

where f_{axion} is the resonant frequency of the mode excited by the axion-photon conversion, and $f_{neighbour}$ is the resonant frequency of the nearest mode.

The findings demonstrate a rapid decline in mode separation as the parameter d/a increases. When the subsequent mode is sufficiently distant in frequency, the form factor reaches its theoretical maximum value for any cavity size, namely $C_{TM_{010}} = 0.6917$ and $C_{TE_{111}} = 0.6783$, derived from equation 1.3.

For a cylindrical cavity, the quality factors of the TM_{mnl} and TE_{mnl} modes can be expressed as [31]

$$Q_{TM_{mnl}} = \begin{cases} \frac{\lambda_0}{\delta_c} \frac{[\chi_{mn}^2 + (l\pi a/d)^2]^{1/2}}{2\pi(1+a/d)}, & l > 0 \\ \frac{\lambda_0}{\delta_c} \frac{\chi_{mn}}{2\pi(1+a/d)}, & l = 0 \end{cases} \quad (2.2)$$

$$Q_{TE_{mnl}} = \frac{\lambda_0}{\delta_c} \frac{\left[1 - \left(\frac{m}{\chi'_{mn}}\right)^2\right] \left[(\chi'_{mn})^2 + \left(\frac{l\pi a}{d}\right)^2\right]^{3/2}}{2\pi \left[(\chi'_{mn})^2 + \frac{2a}{d} \left(\frac{l\pi a}{d}\right)^2 + \left(1 - \frac{2a}{d}\right) \left(\frac{ml\pi a}{\chi'_{mn}d}\right)^2\right]} \quad (2.3)$$

where $\lambda_0 = c/f_r$ is the free-space wavelength of the mode, f_r is the resonant frequency of the cavity mode, $\delta_c = 1/(\sqrt{\pi\mu_0\sigma_c f_r})$ is the skin depth of the cavity surface, μ_0 is the vacuum magnetic permeability, and σ_c is the electrical conductivity of the cavity walls (a

conductivity value of $\sigma_c = 2 \times 10^9$ S/m is adopted, aligning with the characteristics of copper at cryogenic temperatures). By plotting the aforementioned equations (refer to Figures 3a and 3b), it becomes evident that the unloaded quality factor experiences a decline at elevated frequencies in both scenarios, corresponding to a reduction in the cavity radius. Figure 3 allows us to infer that the parameter Q_0 remains unaffected by the cavity length

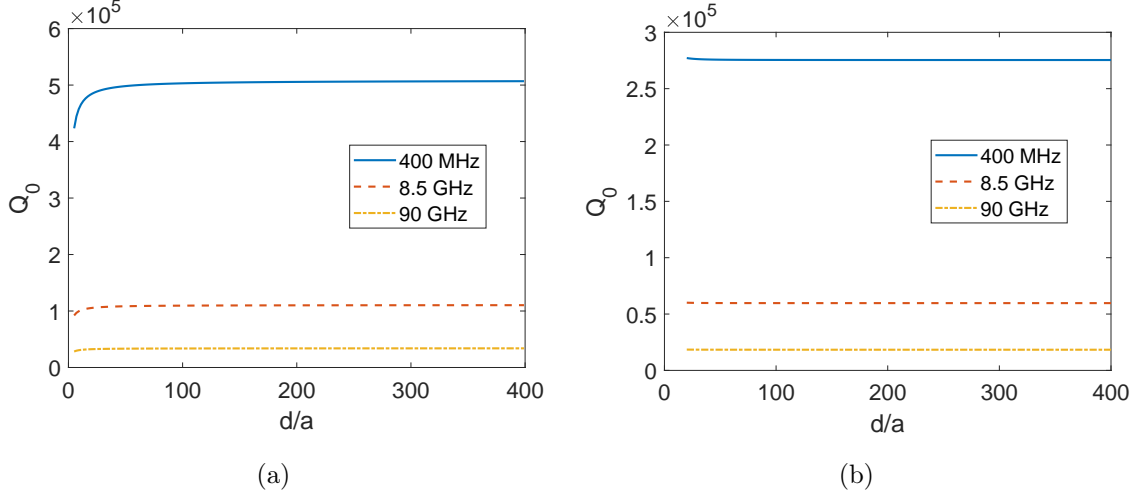


Figure 3: (a) Q_0 of the TM_{mnl} and (b) TE_{mnl} modes as a function of d/a for three frequencies (0.4, 8.4, and 90 GHz).

for high values of d in both modes.

The minimum accepted mode separation (mode clustering) relies on the measured quality factor, which in turn is influenced by the cavity's shape, material, and manufacturing process quality. Higher Q_0 values result in sharper resonances, allowing modes to approach each other in frequency without degradation. Generally, taking a conservative approach, it can be anticipated that the unloaded quality factor of the fabricated prototype will be approximately half of the theoretical value due to manufacturing tolerances in the fabrication process (such as inner wall roughness, soldering quality, and metallic contact in the case of screws usage). To quantify the impact of mode clustering on energy loss, Figures 4a and 4b illustrate the form factor plotted against d/a for various Q_0 values ($Q_0 = 10^4$ for the blue line, $Q_0 = 2 \times 10^4$ for the red line, $Q_0 = 5 \times 10^4$ for the yellow line, and $Q_0 = 10^5$ for the purple line) in the solenoid and dipole scenarios, respectively. This plot demonstrates that higher Q_0 values correspond to a reduced deterioration in C . The form factor presented in Figures 4a and 4b has been computed using equation 1.3, which accounts for the perturbation of the electric field and its resulting impact on C due to the influence of the electric field generated by the adjacent resonant modes (TM_{011} and TE_{112} modes in this case, respectively) when they are in close proximity. The detailed analysis of this phenomenon for rectangular cavities can be found in [16]. Consequently, a constraint must be imposed on the mode separation to achieve a minimum form factor.

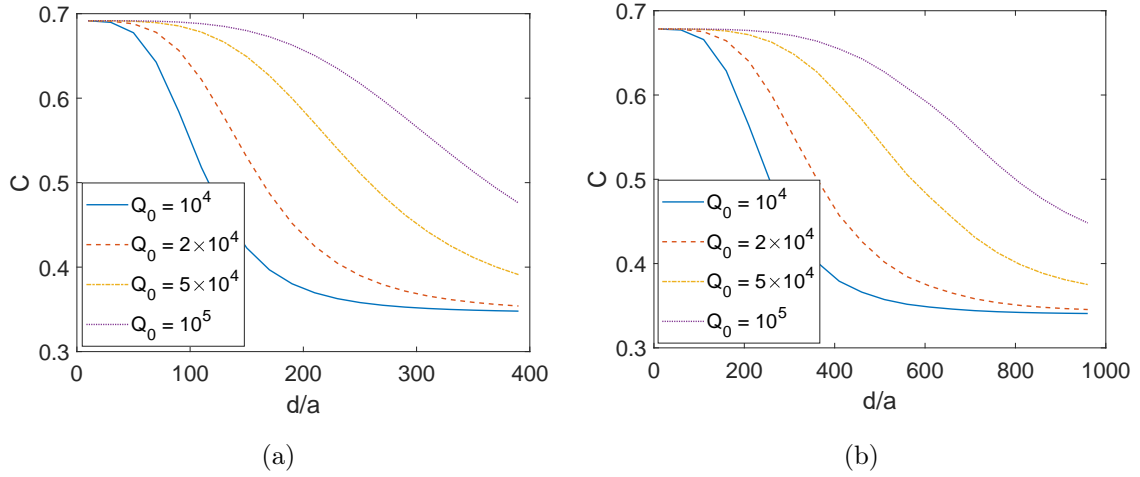


Figure 4: Form factor as a function of the d/a parameter for several Q_0 values for (a) the TM_{010} mode, and (b) the TE_{111} mode.

A maximum form factor reduction of $\sim 1\%$ is chosen as our least allowable lowered value owing to mode clustering. This gives a form factor value of $C = 0.68$ for the TM_{010} mode (solenoid scenario) and $C = 0.67$ for the TE_{111} mode (dipole scenario). The form factor could even be more reduced, but very close modes generate problems in the correct measurement of f_r and Q_0 in the experiment. In any case, if the cavity response has two resonances that are extremely near or even mixed as a result of lower than expected quality factors, there are ways to recover the original form of each resonance and compute the necessary two parameters (f_r and Q_0) [32]. To extract the maximum dimensions, while maintaining these minimum form factor values, the plots from Figures 4a and 4b are analysed for the solenoid and dipole case, respectively.

This form factor minimum value is attained for the X-band situation with the dimensions provided in Table I. These figures are based on an unloaded quality factor after manufacture of half of the theoretical one. The advantages gained with these examples in contrast to WC-109 cylindrical cavities are also shown in Table I. The $Q_0 V^2 C^2$ factors of

Cavity type	Magnet type	$2a$ (mm)	d (mm)	Δf (%)	V (mL)	Q_0	C	$Q_0 V^2 C^2$ (L ²)
Standard	Solenoid	27	26.39	20.27	15.11	7.32×10^4	0.6917	7.996
Standard	Dipole	27.788	26.39	52.96	16.005	7.89×10^4	0.6783	9.299
Long	Solenoid	27	1350	0.009	772.95	10.95×10^4	0.68	3.03×10^4
Long	Dipole	20.67	1395	0.024	468.107	5.97×10^4	0.67	5872

Table I: Comparison of the operational parameters of standard WC-109 cylindrical cavities employed for resonating at 8.5 GHz at both solenoid and dipole scenarios, with very long cavities for the same resonant frequency.

3789 and 632 for the solenoid and dipoles situations, respectively, are significant improvements over the standard WC-109 cavities.

The previous study is an exploration of the dimension limits for a minimal form factor in cylindrical cavities. However, more conservative limits are imposed for the fitting of the cavities inside the magnets taking into account the higher magnet Figure of Merit $FoM = (B_e^2 V)/T$ values. For solenoids, the best case is the MRI-EFR magnet, with $B_{eMRI} = 9$ T, $T_{MRI} = 0.1$ K, $\phi_{MRI} = 800$ mm, and $L_{MRI} = 0.513$ m, giving a $FoM_{MRI} = 215.03 \frac{T^2 m^3}{K}$. For dipoles, the best case will be the BabyIAXO magnet, with $B_{eBI} = 2.5$ T, $T_{BI} = 4.2$ K, $\phi_{BI} = 600$ mm, and $L_{BI} = 10$ m, giving a $FoM_{BI} = 4.207 \frac{T^2 m^3}{K}$.

For the case of a resonant cavity operating with the TE_{111} mode (dipole case), it could fit perfectly into the BabyIAXO magnet using the boundary dimensions shown in Table I ($d = 1.4$ m versus $L_{BI} = 10$ m). However, for the case of a cavity operating with TM_{010} resonant mode (solenoid case), it would have to use a shorter length than shown in Table I to fit the MRI magnet ($d = L_{MRI} = 513$ mm), giving the following parameter values: $\Delta f = 0.059$ %, $V = 293.72$ mL, $Q_0 = 1.08 \times 10^5$, $C = 0.69$, and $Q_0 V^2 C^2 = 4424$ L², which also represent substantial improvements over the standard cavity case.

2.2 Tuning

Various tuning mechanisms are at the disposal for potential adaptation to cylindrical single cavities operating in both solenoid and dipole magnets. For a solenoid scenario, noteworthy among these tuning systems are the mechanical tuning techniques developed by the ADMX group, wherein the manipulation of angular rotations of metal rods serves as a frequency tuning mechanism. This approach has manifested significant outcomes across diverse axion search experiments [17]. The HAYSTAC experimental group has similarly implemented the application of a tuning method based on metallic rods [19]. In addition, the CAPP group has utilized a tuning configuration encompassing the deployment of a single dielectric rod positioned within a cavity. This innovative tuning technique is further enhanced by including a piezoelectric rotational actuator, including the controlled circular movement of the rod installed within the cavity [33].

On the other hand, for dipole magnets, the RADES group has developed a series of experiments based on the exploration of rotary mechanisms employing metallic plates. This investigatory trajectory has been accomplished in the context of long single cavities operating at UHF frequencies, dealing with the mode clustering parameter issue [15]. In addition, the CAPP-CAST group introduced in [26] a mechanical tuning system based on two sapphire strips positioned symmetrically along the longitudinal edges. These strips are adjusted simultaneously, moving towards the centre of the cavity.

The investigation of tuning techniques for cylindrical cavities with large dimensions has been left as future work. This study is envisaged to be developed by the adaptation of the mechanical and electronic methods evidenced in [34] and [35], respectively. It is

important to mention that by introducing tuning in haloscopes, mode clustering will most likely produce significant mode crossings.

3 1D multicavities

The utilization of the multicavity principle in cylindrical haloscope configurations results in a noticeable increase in volume across various spatial orientations including φ , ρ , and z . Importantly, this expansion occurs while maintaining the resonant frequency, a characteristic similar to what has been observed in rectangular multicavity setups [16, 24]. In contrast to the concept of elongated cavities used in dipole magnet arrangements, the multicavity designs oriented along the z -axis exhibit the capability to accommodate larger-diameter cylindrical waveguides. An example of this is the standard WC-109 for X-band frequencies. Additionally, in the CAPP team, an efficient high-frequency haloscope that adopts a multi-cell cylindrical cavity approach was developed and put into operation [36, 37]. This strategy reinforces the volumetric expansion of the haloscopes while preserving the operating frequency.

On the other hand, the RADES team has carried out the development and construction of a series of compact haloscope prototypes with rectangular geometries. Within this effort, versions include an all-inductive configuration that combines five subcavities, as well as two alternating designs featuring different quantities of subcavities ($N = 6$ and $N = 30$, where N represents the number of subcavities). A thorough analysis of these prototypes is presented in a range of works [20, 24, 34, 38, 39].

The Ref. [16] presents an exploration of high-volume structures with rectangular geometries for single cavities and multicavity structures. Similarly, in this paper cylindrical subcavities are analysed taking into account the phenomenon of mode clustering that emerges as the number of subcavities or volume increases [16]. A detailed examination of the three spatial orientations – φ , ρ , and z – for the stacking of cylindrical subcavities to create a multicavity structure has been explored. For each stacking orientation, exemplary designs are discussed presenting the viability of each scenario. Furthermore, an exploration of multicavities with large subcavities is exposed.

3.1 Stacking in φ

The initial configuration analysed in this study involves the arrangement of cylindrical subcavities along the angular axis, often referred to as the φ axis. This arrangement’s specifics are presented through visual aids, as depicted in Figures 5a and 5b. These illustrations show the spatial orientation and structural attributes of two distinct multicavity haloscope models, each incorporating two subcavities. Notably, these prototypes are designed to function within the distinct magnetic settings of solenoid (TM_{010} mode) and dipole (TE_{111} mode) magnets, thus exemplifying a comprehensive exploration of innovative design within diverse experimental contexts. The CAPP group has conducted a series of investigations utilizing structures based on the first configuration, giving significant outcomes [36, 37].

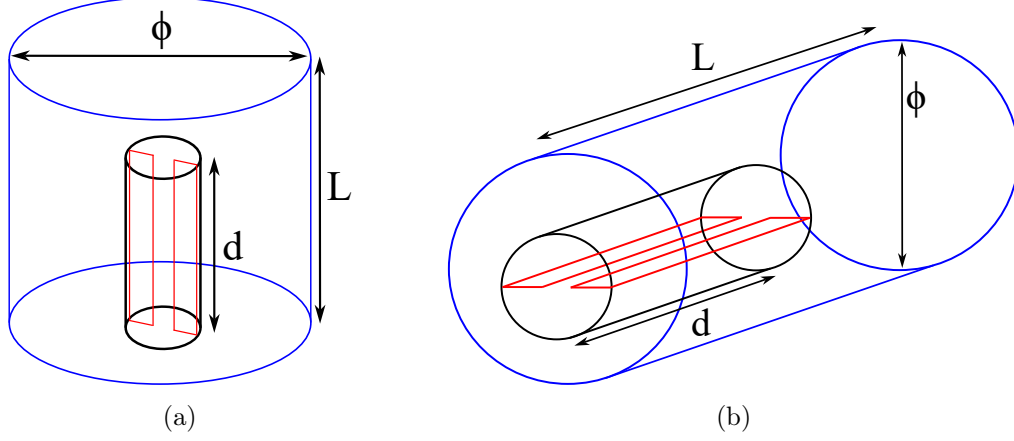


Figure 5: Implementation of multicavity haloscopes of two subcavities (based on a cylindrical cavity divided into two slices) stacked in φ (a) in solenoid and (b) in dipole magnets. The red lines represent the metallic iris windows. The readout antenna for each multicavity design will be located on the upper wall of one subcavity.

Those configurations are based on all inductive iris positioned in the centre of the cylindrical structure. Similarly, in this paper the design and analytical assessment of cylindrical haloscopes interconnecting two subcavities along the φ axis, employing iris manipulation as a main parameter, has been carried out. This multicavity approach takes shape in various arrangements: a central iris placement (as studied by the CAPP group [36]), alongside two additional configurations with irises situated at $1/3$ and $2/3$ of the radial axis, as well as irises situated at both termini of the radial axis. In addition, as a comparison with the case of the centred iris, a design with a centred capacitive iris has been carried out. The graphical renditions of these configurations are depicted through Figure 6, showing the spatial arrangements of the subcavities and their interconnected iris elements.

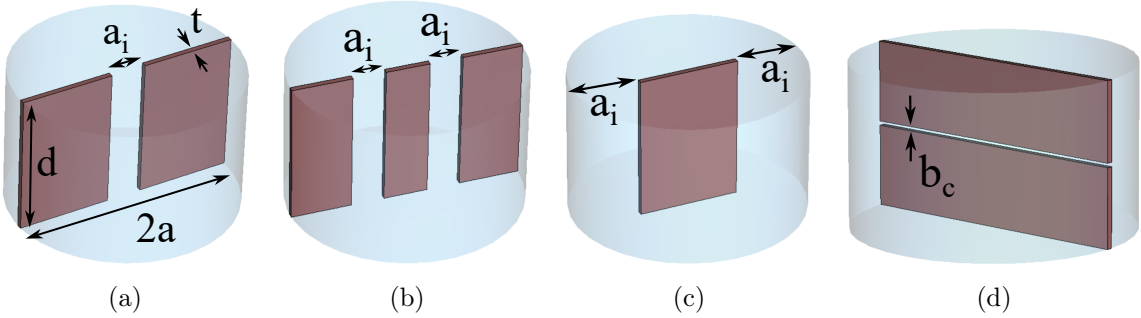


Figure 6: 3D models of the cylindrical haloscopes based on two subcavities varying the inductive iris position along the radial axis: (a) center, (b) $1/3$ and $2/3$ of the diameter, and (c) end. (d) Case with iris in the centre, but capacitive type. a_i and b_c represent the inductive iris width and capacitive iris height, respectively. Light blue solids correspond with resonant cavities and brown solids with metallic iris sections. A thickness value of $t = 1$ mm has been employed for all the cases.

For the design of these structures, the following specifications have been chosen: working frequency of the axion mode $f = 8.5$ GHz, and interresonator coupling $|k| = 0.025$, which implies a mode clustering between the configuration modes ($[+ +]$ and $[+ -]$) of $\Delta f \approx 200$ MHz (or ~ 2.4 %). The results obtained by modifying the position of the inductive iris as mentioned above are collected in Table II. As it can be seen, although the

Type	Iris position	$2a$ (mm)	d (mm)	a_i or b_c (mm)	V (mL)	Q_0	C	$Q_0 V^2 C^2$ (L ²)
Ind.	Center	42.58	26.39	6.8	36.77	6.24×10^4	0.645	35.084
Ind.	1/3 & 2/3	42.55	26.39	6.1	36.85	6.19×10^4	0.665	37.114
Ind.	End	42.7	26.39	12	37.42	5.91×10^4	0.719	42.772
Cap.	Center	45	26.39	0.7	40.88	6.17×10^4	0.558	32.135
Single	-	27	26.39	-	15.11	7.32×10^4	0.6917	7.996

Table II: Comparison of the operational parameters of cylindrical multicavities stacked in φ employed for resonating at 8.5 GHz at solenoid magnets (TM_{010} mode) with $|k| = 0.025$ modifying the inductive iris position in the radial axis. Each case corresponds with the cases showed in Figure 6, except for the last one, which is the single cavity designed in the previous section (see solenoid scenario in Table I).

differences are not very high, we can confirm that the results of the structure with inductive irises at the ends of the radial axis provide a better $Q_0 V^2 C^2$ factor compared to the other two inductive cases analysed. When comparing the inductive iris centred on the radial axis with the capacitive iris centred on the longitudinal axis, we can conclude that the former provides slight improvements.

The inductive and capacitive couplings chosen in this study are based on windows that fill the entire length and diameter of the cavity, respectively. However, other iris designs could be implemented to facilitate the fabrication of prototypes. One example is the replacement of these windows with one or more holes (cylindrical or rectangular in shape, for example). A detailed study of the coupling capability provided by these geometries is necessary in order to extract their practical feasibility.

In relation to the scenario involving the stacking of subcavities along the φ axis, operating in TE_{111} mode and intended for integration onto a dipole magnet, it has revealed a distinctive outcome. In this case, the sole feasible configuration is the example in Figure 5b, characterized by its manifestation within the XZ plane and encompassing a maximum of two subcavities. Unfortunately, the boundary conditions imposed by the inner electrical wall of the iris section have no effect on the electric field of the TE_{111} mode, so the mode is the same as in the original cavity and no increase in resonant frequency is achieved. Consequently, this particular variant of haloscope design can be reasonably omitted from further consideration.

3.2 Stacking in ρ

Illustrated in Figure 7 are examples representative of both solenoids and dipoles, featuring two subcavities that are interconnected along the radial axis. In these cases, we deal with

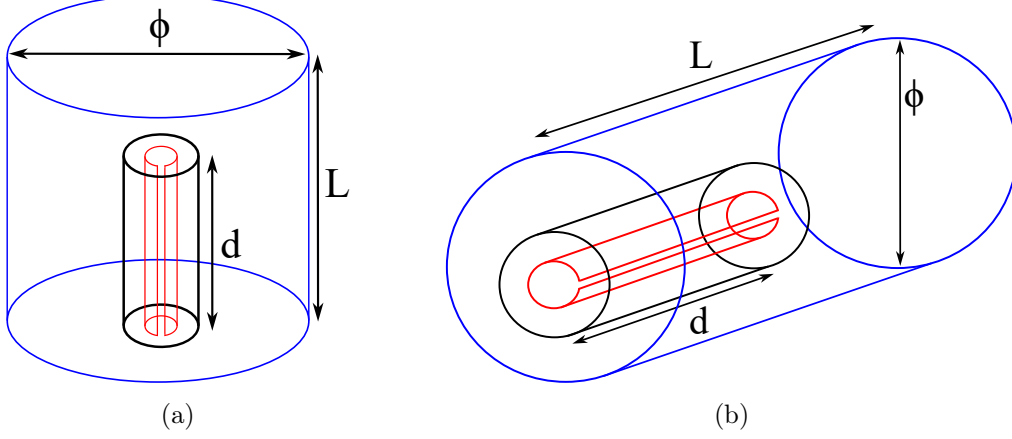


Figure 7: Implementation of multicavity haloscopes of two subcavities stacked in ρ (a) in solenoid and (b) in dipole magnets. The red lines represent the metallic iris windows.

two types of cavities: the inner one is a cylindrical cavity, and the other ones (in the case of N subcavities) are coaxial cavities.

Notably, for the dipole-based configuration, a critical observation has emerged due to disparity in the resonance frequencies associated with the TE_{111} mode between the inner and the outer subcavities. The outer (coaxial) subcavities, configured in a ring-like arrangement, necessitate substantial reduction in size along the radial axis (ρ), leading to a scenario where their resonance frequency cannot be harmonized with that of the inner subcavity. This limitation ultimately renders the feasibility of this particular arrangement unattainable from a practical standpoint. This option is therefore discarded again, as is the case for the φ -stacking case.

Regarding the solenoid configuration, specifically centered on the TM_{010} mode, a thorough investigation has been conducted concerning radial (ρ) couplings involving two subcavities. This study encompasses the incorporation of inductive and capacitive irises, exploring three distinct scenarios contingent on the number of irises: 1, 2, and 4. Figure 8 shows the 3D models of the above-mentioned analysed structures.

For the design of these structures we have set an operating frequency of $f = 8.5$ GHz, and an interresonator coupling of $|k| = 0.025$. Table III shows the outcomes of the studies modifying the type and number of the iris windows. The obtained outcomes demonstrate increased volumetric capacities when compared to both single cavities and φ -coupled configurations, as outlined in Tables I and II. Broadly speaking, the analyzed scenarios share analogous characteristics; nevertheless, it is pertinent to highlight that the configuration

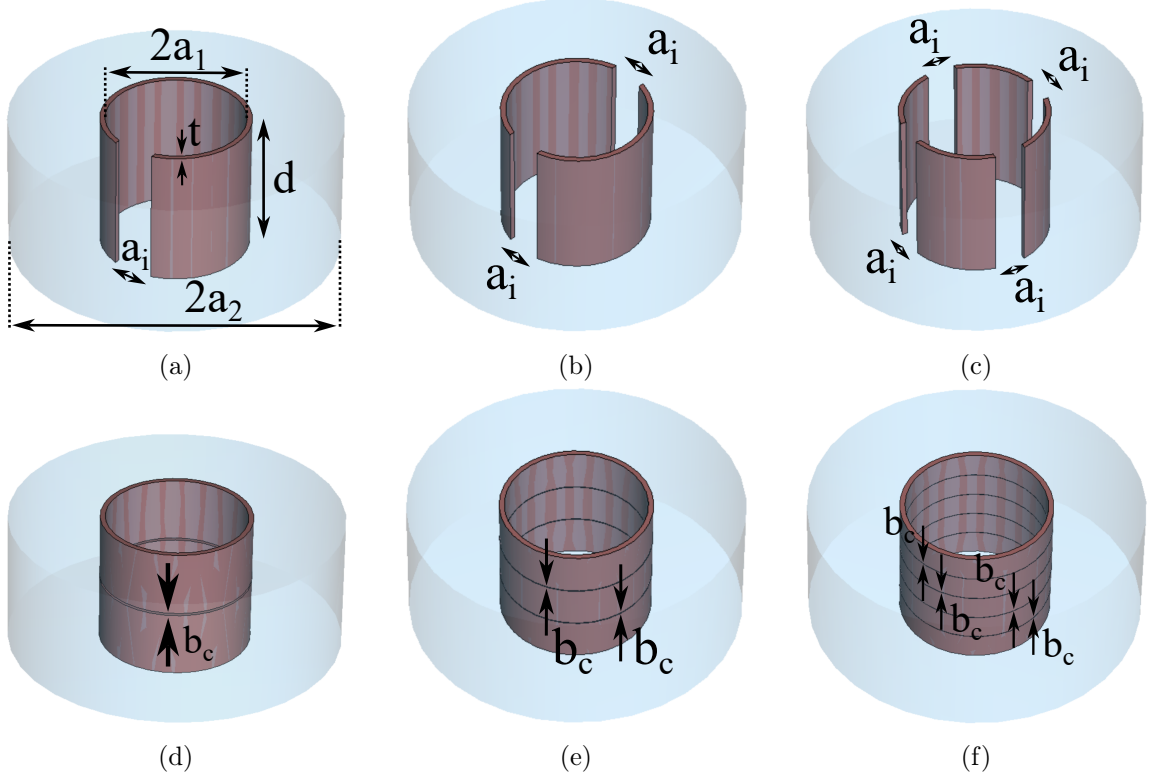


Figure 8: 3D models of the cylindrical haloscopes based on two subcavities varying the type (inductive and capacitive) and number of iris windows stacked in ρ : (a) one inductive iris, (b) two inductive iris, (c) four inductive iris, (d) one capacitive iris, (e) two capacitive iris, and (f) four capacitive iris. a_i and b_c represent the inductive iris width and capacitive iris height, respectively. Light blue solids correspond with resonant cavities and brown solids with metallic iris sections. A thickness value of $t = 1$ mm has been employed for all the cases.

Type	# iris	$2a_1$ (mm)	$2a_2$ (mm)	d (mm)	a_i or b_c (mm)	V (mL)	Q_0	C	$Q_0 V^2 C^2$ (L ²)
Ind.	1	26.3	62.5	26.39	$a_i = 8$	78.97	5.75×10^4	0.582	121.303
Ind.	2	26.2	62.3	26.39	$a_i = 7$	78.53	5.78×10^4	0.687	168.152
Ind.	4	26.15	62.1	26.39	$a_i = 6$	78.69	5.96×10^4	0.65	155.665
Cap.	1	27.85	65.7	26.39	$b_c = 0.5$	87.24	5.78×10^4	0.666	194.957
Cap.	2	27.78	65.55	26.39	$b_c = 0.14$	86.8	5.9×10^4	0.663	195.062
Cap.	4	27.75	65.5	26.39	$b_c = 0.06$	86.4	5.92×10^4	0.649	186.017
Single	-	$2a = 27$	-	26.39	-	15.11	7.32×10^4	0.6917	7.996

Table III: Comparison of the operational parameters of cylindrical multicavities stacked in ρ employed for resonating at 8.5 GHz at solenoid magnets (TM_{010} mode) with $|k| = 0.025$ modifying the type and number of iris windows. Each case corresponds with the cases showed in Figure 8, except for the last one, which is the single cavity designed in the previous section (see solenoid scenario in Table I).

featuring a solitary inductive iris exhibits a diminished form factor due to its asymmetrical geometry. Additionally, it is affirmed that structures incorporating capacitive irises offer superior $Q_0V^2C^2$ factors. However, it is noteworthy that the latter configurations encounter certain structural complexities, the exploration of which is reserved for future investigations¹.

As commented in the φ -stacking case, the selection of inductive and capacitive couplings in this investigation is grounded in windows that span the entire length and φ of the cavity, respectively. Nevertheless, as with the φ -stacked scenario, alternative iris configurations could be employed to simplify prototype fabrication. One instance involves substituting these windows with one or more perforations. An exhaustive examination of the coupling potential offered by these geometries is essential to assess their practical viability.

3.3 Stacking in length

Regarding the situation of length-coupled (z axis) configurations (as observed in the instances with solenoid and dipole magnets in Figures 9a and 9b, respectively), the examination closely mirrors the approach undertaken for rectangular designs as documented in [16].

To validate the viability of cylindrical configurations, a demonstration has been presented through the design (with $f = 8.5$ GHz and $|k| = 0.025$) of two multicavity haloscopes, each consisting of a pair of subcavities. These designs address both solenoid and dipole magnets, integrating an inductive iris as depicted in Figures 9c and 9d, respectively. In the case of the solenoid setup (TM_{010} mode), a rectangular iris has been implemented, while the dipole configuration (TE_{111} mode) incorporates an elliptical iris, which gives better results in quality factor and manufacturing possibilities [40]. The outcomes of the simulations are illustrated in Table IV. They reveal consistently favorable results for both scenarios. The achieved $Q_0V^2C^2$ factor is over threefold superior compared to outcomes from conventional single cavity designs, demonstrating the enhancement brought about by the multicavity approach in cylindrical structures. When considering the operation in the context of a solenoid magnet and the TM_{010} mode, outcomes are slightly worse than those observed in the φ and ρ stacking configurations. Nevertheless, unlike these two stacking methods, length (z) coupling remains a feasible option for the TE_{111} mode when operating within a dipole magnet configuration.

3.4 Possibilities for increasing the subcavity volume

Furthermore, alongside the investigation of subcavity stacking within cylindrical waveguide configurations, an extended exploration has been conducted involving multicavity arrangements characterized by large dimensions. This expansion aims to facilitate an augmentation of volume and, in some cases, the improvement of quality factors, consequently amplifying the $Q_0V^2C^2$ factor. To ensure compatibility in terms of spatial dimensions, the analyses

¹The cases with 2 and 4 capacitive irises have to be slightly modified to make them manufacturable. These modifications consist of replacing the full horizontal apertures on the φ axis by partial gaps, adding junctions between the consecutive capacitive sections in z axis.

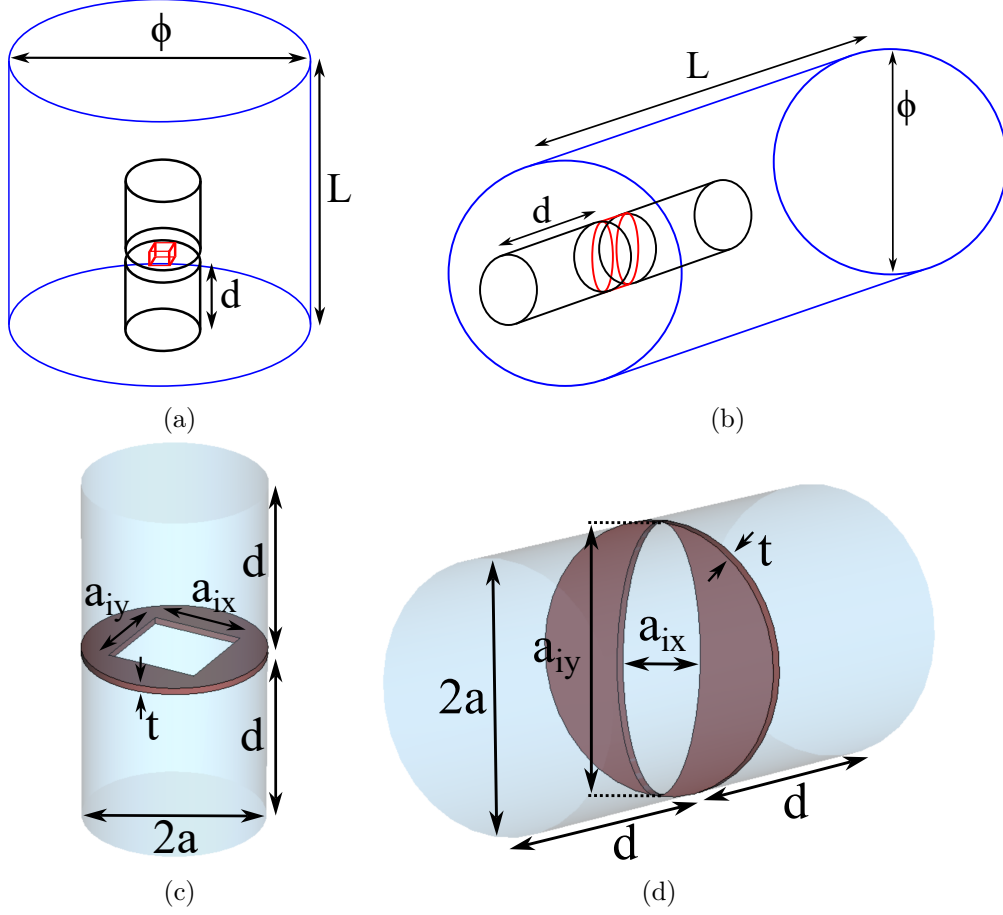


Figure 9: Implementation of two cylindrical subcavities stacked in length (a) in solenoid and (b) in dipole magnets. The red lines represent the metallic iris windows. 3D models of these cylindrical haloscopes for (c) solenoid and (d) dipole magnet. Light blue solids correspond with resonant cavities and brown solids with metallic iris sections. A thickness value of $t = 1$ mm has been employed for both cases.

Type	$2a$ (mm)	d (mm)	a_{ix} (mm)	a_{iy} (mm)	V (mL)	Q_0	C	$Q_0 V^2 C^2$ (L ²)
Solenoid (z stacking)	27.1	26.39	14	14	30.44	7.44×10^4	0.691	32.953
Dipole (z stacking)	26.4	26.39	4.8	26.4	28.64	7.4×10^4	0.709	30.59
Solenoid (sing. cav.)	27	26.39	-	-	15.11	7.32×10^4	0.6917	7.996
Dipole (sing. cav.)	27.788	26.39	-	-	16.01	7.89×10^4	0.6783	9.299

Table IV: Comparison of the operational parameters of cylindrical multicavities stacked in z employed for resonating at 8.5 GHz at solenoid (TM_{010} mode) and dipole (TE_{111} mode) magnets with $|k| = 0.025$ with an inductive iris. Each case corresponds with the cases showed in Figures 9c and 9d, except for the last two ones, which are the single cavities designed for solenoid and dipole scenarios in the previous section (see Table I).

have been based on the largest magnets examined in the prior research [16]. Specifically, the focal points of this study encompass the quasi-dipole BabyIAXO magnet (considered

here as dipole magnet, for simplicity), and the MRI (ADMX-EFR) solenoid magnet.

The methodology employed in these investigations has involved augmenting the dimensions of the subcavities examined in the preceding three sections (one representative case from each stacking type and magnet configuration). To achieve an increase in volume, it becomes necessary to amplify either the length (d) or the radius (a), a modification that can lead to the proximity of higher order modes. Such considerations necessitate an assessment of the mode clustering factor to prevent the diminishment of the form factor and the introduction of complexity in the computation of parameters f_r and Q_0 .

3.4.1 Long subcavities

To exemplify the potential of volumetric expansion through length adjustments in cylindrical multicavity configurations, a series of four distinct structures were analysed. In all cases, a subcavity length of $d = 100$ mm was employed. Initially, the structure depicted in Figure 6a was selected, a haloscope featuring two subcavities operating in the TM_{010} mode situated within a solenoid magnet, and arranged in a φ -stacked configuration with a centrally positioned inductive iris. Subsequently, the design process was extended to encompass the structure illustrated in Figure 8b, characterized by two elongated subcavities operating in a solenoid magnet stacked along the ρ axis and equipped with two inductive irises. Lastly, the design of the two structures presented in Figures 9c and 9d (stacked along the length axis) was undertaken, representing both solenoid and dipole configurations, respectively.

The outcomes ensuing from the application of a 100 mm subcavity length and the subsequent reoptimization of dimensions to sustain operation at 8.5 GHz with $|k| = 0.025$ for the first two scenarios (Figures 6a and 8b) are illustrated in Table V. The outcomes

Case (stacking and magnet)	$2a$ (mm)	d (mm)	a_i (mm)	V (mL)	Q_0	C	$Q_0 V^2 C^2$ (L ²)
φ and solenoid (Figure 6a)	42.63	100	7	139.67	7.98×10^4	0.648	652.381
ρ and solenoid (Figure 8b)	$2a_1 = 26.2$	100	7.8	300.15	7.11×10^4	0.668	2857.09
	$2a_2 = 62.3$						

Table V: Comparison of the operational parameters of cylindrical long multicavities for stacking in φ , ρ and z . For the last one, both solenoid and dipole scenarios are shown. The designs are optimized for resonating at 8.5 GHz with $|k| = 0.025$ with inductive iris windows.

achieved demonstrate that augmenting the length of these configurations by a factor of 4 has yielded a notable enhancement of the $Q_0 V^2 C^2$ factor, exceeding 18-fold improvement (see Tables II and III). Furthermore, in these specific cases, it has been determined that the higher-order mode TM_{011} has drawn closer (owing to the extension in d), now exhibiting a slightly closer proximity to the axion mode than the configuration mode $[+ -]$ of TM_{010} . As a result, it becomes necessary to analyse this aspect when calculating the parameter Δf (even though, for these instances, the decrease in the form factor remains negligible due to

the substantial separation between adjacent modes). This result presents a compelling and promising trajectory for the formulation of extended haloscope designs taking advantage of these stacking methodologies.

Regrettably, while endeavoring to implement a length of 100 mm in the length-stacked scenarios (Figures 9c and 9d), a constraint in the iris aperture has been identified. In the case of solenoid configuration (TM_{010} mode) an upper threshold of approximately $d = 33$ mm has been established, surpassing which the iris becomes unable to widen adequately to facilitate the requisite coupling. For the dipole scenario (TE_{111} mode) this statement materializes at the boundary of $d = 60$ mm. This limitation aligns quite closely with the findings in the research outlined in [16] for multicavities of rectangular shape. Therefore, once this limit in length is reached, the only way to continue augmenting in volume is by increasing the number of subcavities.

3.4.2 Large diameter subcavities

In contrast to the longitudinal dimension (d), structures operating in the TM_{010} resonant mode (for solenoid magnets) necessitate a precise radius (a) value due to the direct dependence of the resonance frequency on this parameter. As a result, expanding this dimension is not feasible for solenoid-type configurations. However, for multicavity structures of the dipole type (TE_{111} mode), the radius can indeed be augmented. As observed in the preceding sections, only the length-coupled scenario exists. To exemplify this concept, the design of a structure based on two interconnected subcavities with an elliptical iris (see Figure 9d) featuring significantly larger radii has been undertaken. For this case, a diameter of $2a = 100$ mm has been chosen. This structure has been configured to operate at a frequency of 8.5 GHz with an interresonator coupling of $|k| = 0.025$. The results derived from this particular design are presented in Table VI. It is noteworthy to highlight

Case (stacking and magnet)	$2a$ (mm)	d (mm)	a_i (mm)	V (mL)	Q_0	C	$Q_0 V^2 C^2$ (L ²)
z and dipole (Figure 9d)	100	17.48	$a_{ix} = 4.8$ $a_{iy} = 100$	272.43	6.92×10^4	0.574	1693.101

Table VI: Operational parameters of a cylindrical multicavity with large diameter subcavities stacked in z with an elliptical iris windows, operating at a dipole magnet (TE_{111} mode). The prototype works at 8.5 GHz with $|k| = 0.025$.

the substantial decrease in the cavity length required for tuning the resonance frequency in comparison to the newly set diameter. Additionally, a considerable augmentation in volume is evident when compared to the standard diameter configuration (refer to Table IV). Consequently, for this specific situation, it can be inferred that a fourfold increase in diameter leads to a remarkable enhancement in the $Q_0 V^2 C^2$ by over 55 times. This outcome once again presents a promising avenue to leverage a variety of dipole-type magnets.

Unfortunately, an issue arises when there is the potential for TM modes to transition into TE_{111} mode as the cavity radius experiences a substantial increase, particularly at

high frequencies such as W-Band. In these instances, the phenomenon of mode mixing can present challenges, as the frequency crossings during tuning can become quite numerous. This situation could lead to complications in accurately determining the parameters f_r and Q_0 , and there might be a risk of diminished form factor. Therefore, when undertaking the design of structures of this nature, it becomes imperative to exercise meticulous caution and consideration regarding these mode transitions in the haloscope response.

Regarding structures tailored for solenoid magnets with either φ or ρ coupling, a somewhat distinct approach can be adopted. For a fully utilization of the magnet’s diameter (for instance, the 800 mm diameter of the MRI magnet [16]), one can opt for an overall haloscope diameter that aligns with that of the magnet. Subsequently, the required number of radial subcavities can be implemented to attain the desired resonant frequency. This approach is tenable due to the general trend of higher resonance frequencies corresponding to smaller volumes (as indicated by equation 1.5).

3.5 Tuning

The tuning mechanisms elucidated in section 2.2 for single cavities can be similarly adapted for the context of cylindrical structures based on 1D multicavities. The CAPP group has conducted investigations wherein dielectric rods were employed to tune cylindrical 1D multicavities in solenoids with 2, 4, 6, and 8 subcavities coupled in the φ direction driven by an inductive central iris [37].

Furthermore, endeavors are currently in progress within the RADES group to implement the tuning systems detailed in [15] (based on metal rotation plates) for 1D cylindrical multicavities operating at dipole magnets. In the same line, a haloscope operating at 213.6 MHz (UHF-band) with the TE_{111} mode (scenario for a dipole magnet) based on 8 subcavities coupled in the longitudinal axis through elliptical irises (see Figure 9d) has been studied where a metallic frequency tuning plate has been incorporated (see Figure 10). The

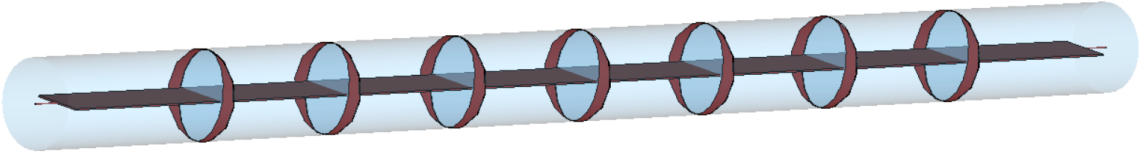


Figure 10: 3D model of a metallic plate system for frequency tuning implemented in a haloscope based on 8 subcavities interconnected by elliptical irises in the longitudinal axis.

first simulations have provided interesting results by a total plate rotation of 60° leading to a tuning range of 8 MHz (3.74 %), with form and quality factors within the $[0.055, 0.321]$ and $[1.31 \times 10^5, 1.32 \times 10^5]$ ranges, respectively. The development of this particular aspect of research has been assigned as a future avenue of exploration.

4 2D and 3D multicavities

This study has delved into the utilization of multiple stacking axes, encompassing structures of 2D or 3D configurations. As elucidated in preceding sections, the possibility of stacking in φ and ρ arises exclusively for multicavities operating under the TM_{010} mode (pertaining to the solenoid magnet context). Consequently, for 2D/3D multicavities, only this mode of operation remains tenable. As a consequence, the subsequent combinations have been subject to exploration: φ and ρ (2D), φ and z (2D), ρ and z (2D), and φ , ρ , and z (3D).

4.1 Stacking in φ and ρ

For this initial configuration, any permutation of inductive and capacitive irises, as expounded in sections 3.1 and 3.2, could be selected. To substantiate this principle, the formulation of a 2D structure has been executed as a proof of concept. To streamline the study, an all-inductive iris configuration has been reselected for the multicavity. Moreover, concerning coupling at φ the configuration featuring two irises at the termini has been opted for (refer to Figure 6c). Conversely, for coupling in ρ , a symmetric dual iris configuration has been chosen (refer to Figure 8b). The three-dimensional representation of this structure is depicted in Figure 11. After an optimization process modifying slightly the dimension

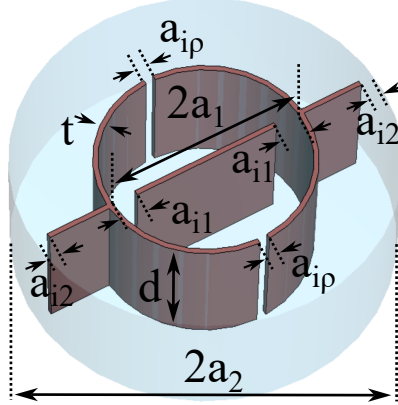


Figure 11: 3D model of a 2D multicavity employing φ and ρ stacking for operation at solenoid magnets. Light blue solids correspond with resonant cavities and brown solids with metallic iris sections. An iris section thickness of $t = 1$ mm has been selected.

values shown in Figure 11 the outcomes presented in Table VII have been determined. This

Case (stacking and magnet)	$2a$ (mm)	d (mm)	a_i (mm)	V (mL)	Q_0	C	$Q_0 V^2 C^2$ (L ²)
φ & ρ and solenoid	$2a_1 = 81.1$	26.39	$a_{i1} = 9$	129.28	5.48×10^4	0.669	409.633
	$2a_2 = 43.6$		$a_{i2} = 14$				
			$a_{i\rho} = 2$				

Table VII: Operational parameters of a 2D cylindrical multicavity stacked in φ and ρ operating at a solenoid magnet (TM_{010} mode).

particular configuration has been developed to operate at approximately 8.494 GHz. A

mode clustering parameter of approximately $\Delta f = 5.6$ MHz has been achieved.

It can be affirmed that the outcomes achieved in relation to the volume and $Q_0 V^2 C^2$ factor surpass, those obtained for 1D multicavities, as evidenced by the data in Tables II and III.

4.2 Stacking in φ and length

An analogous approach to the previously discussed section has been undertaken for 2D cylindrical multicavities coupled along the φ and z axes. In this instance, the configuration depicted in Figure 12 has been devised as the basis for the haloscope. The design employs

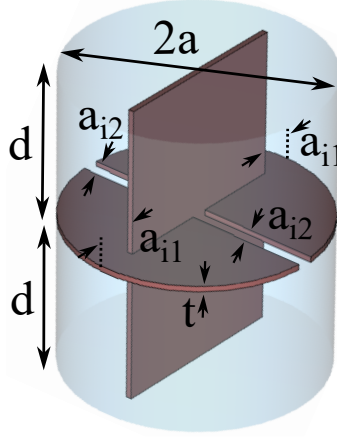


Figure 12: 3D model of a 2D multicavity employing φ and z stacking for operation at solenoid magnets. Light blue solids correspond with resonant cavities and brown solids with metallic iris sections. An iris section thickness of $t = 1$ mm has been selected.

an all-inductive setup. When it comes to coupling along the φ axis, dual irises have been positioned at the extremities, while for the lengthwise coupling rectangular inductive irises have been selected (similar to the scenarios depicted in Figure 9). The optimization process has yielded to the simulation results presented in Table VIII. This specific arrangement has

Case (stacking and magnet)	$2a$ (mm)	d (mm)	a_i (mm)	V (mL)	Q_0	C	$Q_0 V^2 C^2$ (L ²)
φ & z and solenoid	43.86	26.39	$a_{i1} = 6.5$ $a_{i2} = 4$	78.85	6.58×10^4	0.646	171.02

Table VIII: Operational parameters of a 2D cylindrical multicavity stacked in φ and z operating at a solenoid magnet (TM_{010} mode).

been devised to operate at approximately 8.496 GHz. An achieved mode clustering parameter of roughly $\Delta f = 7$ MHz has been observed. Notably, the optimization stage has produced a highly favourable form factor value.

The results clearly indicate that the achieved $Q_0V^2C^2$ factor improvements exceed those obtained for 1D multicavities, as illustrated by the data presented in Tables II and IV, resulting in an increase of its value by over fourfold.

4.3 Stacking in ρ and length

The final feasible arrangement for 2D multicavities involves the utilization of the ρ and z axes to stack subcavities. In this scenario, the prototype design features symmetrical inductive irises for coupling along the ρ axis and ring-shaped inductive irises for coupling along the length axis, as depicted in Figure 13². After an optimization process modifying

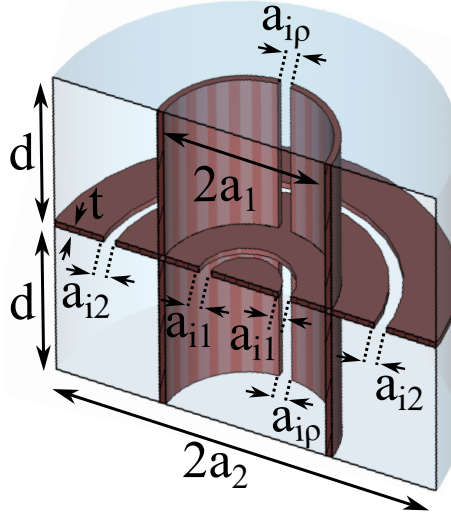


Figure 13: 3D model of the symmetrical half of a 2D multicavity employing ρ and z stacking for operation at solenoid magnets. Light blue solids correspond with resonant cavities and brown solids with metallic iris sections. An iris section thickness of $t = 1$ mm has been selected.

slightly the dimension values of the structure, the results outlined in Table IX have been obtained. This specific arrangement has been developed for operation around 8.496 GHz.

Case (stacking and magnet)	$2a$ (mm)	d (mm)	a_i (mm)	V (mL)	Q_0	C	$Q_0V^2C^2$ (L ²)
ρ & z and solenoid	$2a_1 = 26.95$ $2a_2 = 63.95$	26.39	$a_{i1} = 2$ $a_{i2} = 2.5$ $a_{ip} = 2.5$	165.41	6.33×10^4	0.629	685.84

Table IX: Operational parameters of a 2D cylindrical multicavity stacked in ρ and z operating at a solenoid magnet (TM_{010} mode).

An achieved mode clustering parameter of approximately $\Delta f = 7.4$ MHz has been observed.

²Comparable to certain designs depicted in Figure 8, slight adjustments to the inner inductive coupling ring of this 2D multicavity are envisioned to render it feasible, replacing the iris window by partial apertures.

It is worth noting that the results achieved in terms of $Q_0V^2C^2$ factor outperform significantly those obtained for 1D multicavities, as indicated by the data presented in Tables III and IV.

4.4 Stacking in φ , ρ , and length

In order to construct 3D multicavity structures, the integration of various stacking orientations among subcavities is essential, encompassing coupling along the φ , ρ , and z axes. A prototype design featuring eight subcavities incorporating all inductive irises has been formulated to serve as a demonstration of the viability of such haloscopes. In the context of φ coupling, the selection involves two irises situated at the extremities. For the ρ stacking, a pair of symmetrical irises is employed. Lastly, coupling along the longitudinal axis involves the utilization of two ring-shaped iris windows, as depicted in Figure 14. As

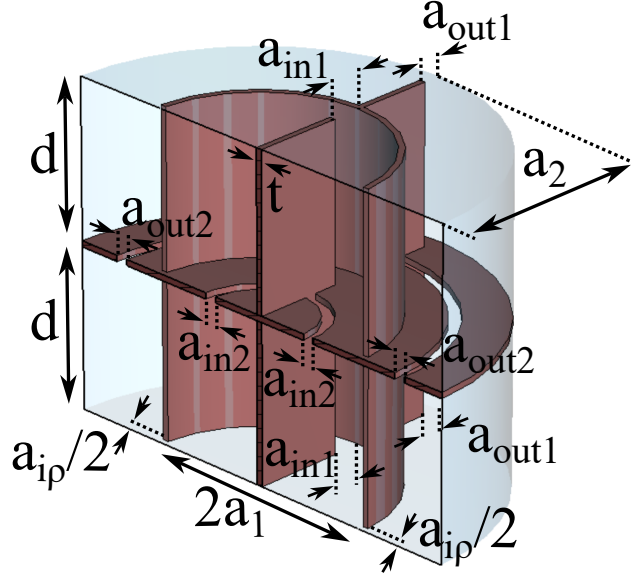


Figure 14: 3D model of the symmetrical half of a 3D multicavity employing φ , ρ , and z stacking for operation at solenoid magnets. Light blue solids correspond with resonant cavities and brown solids with metallic iris sections. An iris section thickness of $t = 1$ mm has been selected.

evident, the quantity of parameters requiring optimization has substantially expanded, consequently making the design process for this structure potentially complex. However, after a fine optimization, the simulation results detailed in Table X have been achieved. This particular configuration has been designed for operation at approximately 8.501 GHz. A mode clustering parameter of around $\Delta f = 4$ MHz has been attained.

Upon comparing these findings with the examined 2D structures (see Tables VII, VIII and IX), it is evident that the acquired $Q_0V^2C^2$ factor is better, confirming the feasibility of 3D geometries in cylindrical multicavity haloscopes.

Case (stacking and magnet)	$2a$ (mm)	d (mm)	a_i (mm)	V (mL)	Q_0	C	$Q_0 V^2 C^2$ (L ²)
φ , ρ & z and solenoid	$2a_1 = 43.6$ $2a_2 = 81.1$	26.39	$a_{in1} = 9$ $a_{out1} = 14$ $a_{i\rho} = 2$ $a_{in2} = 2$ $a_{out2} = 2.5$	264.51	6.08×10^4	0.553	1299.02

Table X: Operational parameters of a 3D cylindrical multicavity stacked in φ , ρ , and z operating at a solenoid magnet (TM_{010} mode).

4.5 Hexagonal multicavities

Another concept briefly introduced consists of the employment of resonant cavities with hexagonal section for the constitution of 2D and 3D multicavity haloscope structures. This hexagonal spatial arrangement is distinguished as an optimally efficient approach for populating structures with circular geometry, thus optimizing the volumetric occupancy. The articulation of this notion has been previously introduced in a prior publication [41] wherein hexagonal single cavities positioned adjacently within a common magnet, to be in-phase added by means of power combiners, were subjected to analysis and evaluation.

As previously stated, the conceptualization of 2D and 3D configurations is practically attainable solely for the TM_{010} mode, primarily within solenoid magnet scenarios. Hence, the scope of this investigation pertains exclusively to this resonant mode for the designated structures. Within this paper, preliminary prototypes for 2D and 3D multicavities employing hexagonally structured subcavities have been formulated. In this analysis, the initial phase involves the design and optimization of an individual cavity of hexagonal geometry operating at 8.5 GHz. A 3D model of this cavity is illustrated in Figure 15a. The ensuing

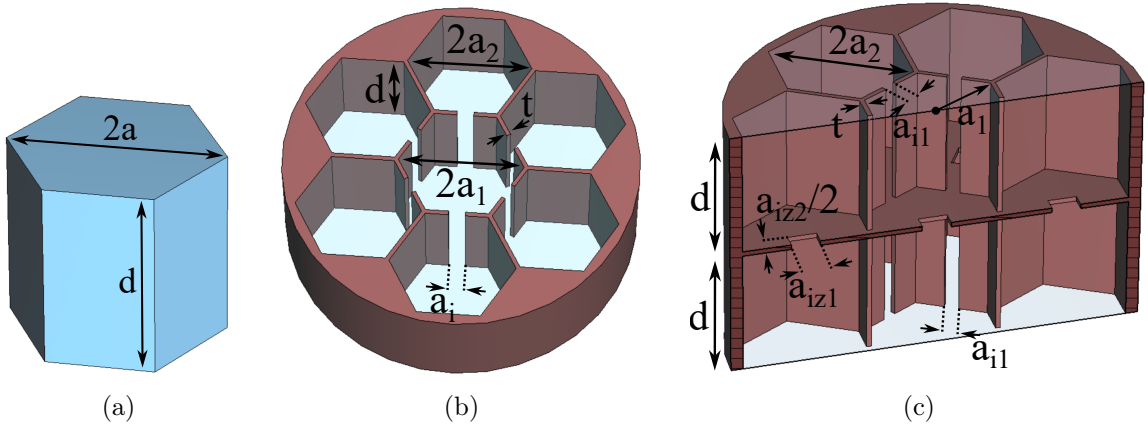


Figure 15: 3D models of hexagonal haloscopes for solenoid magnets: (a) single cavity, (b) 2D multicavity of 7 subcavities, and (c) 3D multicavity of 14 subcavities. In (b) and (c), light blue solids correspond with resonant cavities and brown solids with metallic iris sections. In (c), the symmetrical half of the structures is depicted. A thickness value of $t = 1.5$ mm has been employed for all the scenarios.

results of this preliminary endeavor are documented in Table XI. The outcomes are indicative of similar $Q_0V^2C^2$ factor values when compared with the data presented in Table I for a single circular cavity (solenoid magnet case).

Case and magnet	$2a$ (mm)	d (mm)	a_i (mm)	V (mL)	Q_0	C	$Q_0V^2C^2$ (L ²)
Single cav. and solenoid	30	26.39	—	15.4	7.13×10^4	0.682	7.875
2D multicav. and solenoid	$2a_1 = 29.15$ $2a_2 = 29.95$	26.39	3.4	108.1	7.19×10^4	0.622	324.82
3D multicav. and solenoid	$2a_1 = 29.15$ $2a_2 = 29.95$	26.39	$a_i = 3.4$ $a_{iz1} = 6$ $a_{iz2} = 6$	213.61	7.22×10^4	0.625	1284.3

Table XI: Comparison of the operational parameters of a hexagonal single cavity, and 2D and 3D multicavities in a solenoid magnet (TM_{010} mode).

Using these numerical values as a basis, a duplication of the hexagonal resonator has been undertaken to construct a two-dimensional multicavity configuration consisting of seven subcavities. These subcavities are interconnected to the central cavity using inductive irises that are symmetrically positioned on the sidewalls, as depicted in Figure 15b. Applying fine refinement in simulation, the dimensions and outcomes summarized in Table XI have been achieved. The resulting resonant frequency for this configuration stands at 8.49 GHz, accompanied by a mode clustering value of approximately $\Delta f = 13$ MHz. It can be verified that the achieved $Q_0V^2C^2$ factor has notably expanded when compared to the hexagonal single cavity scenario. In a comparative analysis with the 2D case documented in Table VII (pertaining to stacking along the φ and ρ axes), the achieved volume may appear slightly lower, yet the quality factor have experienced a considerable increase. This increase in the quality factor suggests that the potential for enhanced $Q_0V^2C^2$ factor is plausible following optimization efforts increasing the form factor value.

Concluding this investigation, a further examination was conducted involving the duplication of the previously detailed structure along its length, leading to the creation of a 3D multicavity configuration. This 3D construct is comprised of 14 hexagonal subcavities, each interconnected through inductive irises. All of these irises adhere to an inductive configuration. In the case of length-wise coupling, a selection was made in favour of centrally positioned square-shaped irises, as visually represented in Figure 15c. The outcomes yielded by several optimization iterations are presented in Table XI. Specifically, the resonance frequency corresponding to this design registers at 8.502 GHz, and the accompanying mode clustering value amounts to approximately $\Delta f = 12$ MHz.

As evident from the data, the reached $Q_0V^2C^2$ factor for this configuration closely aligns with that of the 3D structure devised for cylindrical cavities, as outlined in Table X. Nevertheless, it is worth noting that the design and optimization process of this structure is significantly simpler than the cylindrical scenario, due to the number of variables to be optimised. Hence, it can be asserted that the adoption of hexagonal resonant cavities presents

an alternative approach for fabricating high-volume haloscopes through the implementation of multicavity configurations suitable for integration within solenoid magnets.

4.6 Tuning

The techniques for adjusting resonant frequencies discussed in sections 2.2 and 3.5 for single cavities and 1D multicavities can be similarly applied to the context of cylindrical or hexagonal structures based on 2D or 3D multicavities. The ADMX group has introduced a hybrid tuning system concept in [41] which involves employing dielectric films and mechanical adjustments to tune hexagonal 2D and 3D multicavities.

In this case, individual tuning can be realized at each cavity, following the procedure described in [33]. Nevertheless, tuning procedure for a multicavity is much more complex, since only the multicavity resonance is monitored.

5 Conclusions and prospects

This research delves into the exploration of volume limitations in cylindrical haloscopes. The enhancement of this parameter yields improvements in the $Q_0V^2C^2$, a well-known figure of merit of cavity haloscopes, thereby ultimately enhancing the scanning rate. Various strategies for augmenting the volume are presented, with considerations for constraints such as mode clustering which refers to the separation between adjacent modes, and the behaviour of form and quality factors. The study encompasses comprehensive investigations involving single cavities, 1D multicavities, and 2D and 3D multicavities that achieve significant $Q_0V^2C^2$ factors. The feasibility of implementing these haloscopes with the most substantial dipole and solenoid magnets in the axion community is demonstrated. The practical implementations of several designs yield favourable outcomes in quality factor, form factor, and mode clustering, effectively showcasing the potential of these studies while also validating their efficacy.

Among the various types of single cavities explored, it has been determined that large cavities operating within solenoid magnets (TM_{010} mode) exhibit the most favorable performance in terms of the $Q_0V^2C^2$ figure of merit. Additionally, the utilization of multicavities, despite their increased design complexity has been demonstrated to enhance this factor. However, it is noted that the quest for increased volume to cover a range of axion masses is restricted by the permissible number of mode crossings. In the context of 1D multicavities, the feasibility of stacking in φ and ρ orientations for dipole magnets is found to be impractical. Among the extensive designs of large 1D multicavities conducted for solenoids, the structures stacked in ρ orientation manifest the most favourable outcomes in terms of the $Q_0V^2C^2$ factor. For 2D multicavities, the alternative with the best figure of merit results is the haloscope stacked in ρ and length. The 3D structure analysed has given very positive results in terms of $Q_0V^2C^2$ factor, exceeding the values of the single, 2D and 3D cases. In addition, a study with a single cavity, a 2D multicavity and a 3D multicavity for hexagonal geometry has been carried out, providing similar results to the cylindrical

structures, but with simpler design and optimisation processes. These methodologies are intended to provide a practical guide for experimental axion research groups embarking on the pursuit of volume limits in the development of haloscopes based on cylindrical or hexagonal cavities, positioned within both dipole and solenoid magnets. Nevertheless, these approaches and analyses hold relevance for any scenario where augmenting the volume of the device at a specific frequency constitutes an objective.

This analysis opens up a range of promising strategies depending on the nature and configuration of the experiment magnet. The methodologies outlined in this research provide avenues to maximise the potential of magnet spacing, with the overall goal of refining the sensitivity and scanning rate of axion detection. In this sense, it is highly recommended to embark on exploring the limits of cylindrical geometries, taking advantage of various concepts proposed in this study. Examples include the incorporation of alternating couplings in 1D, 2D and 3D multicavities, as well as the implementation of elongated subcavities in 2D and 3D multicavities. In addition, envisaged exploration for the generalization for N subcavities and in-depth analysis of different tuning procedures for multicavities is expected.

Acknowledgments

This work was performed within the RADES group. We thank our colleagues for their support. It has been funded by MCIN/AEI/10.13039/501100011033/ and by “ERDF A way of making Europe”, under grants PID2019-108122GB-C33 and PID2022-137268NB-C53. JMGB thanks the grant FPI BES-2017-079787, funded by MCIN/AEI/10.13039/501100011033 and by "ESF Investing in your future", the European Research Council grant ERC-2018-StG-802836 (AxScale project), and the Lise Meitner program "In search of a new, light physics" of the Max Planck society. This article is based upon work from COST Action COSMIC WISPer CA21106, supported by COST (European Cooperation in Science and Technology).

References

- [1] S. Weinberg, *A new light boson?*, [*Phys. Rev. Lett.* **40** \(1978\) 223](#).
- [2] F. Wilczek, *Problem of strong P and T invariance in the presence of instantons*, [*Phys. Rev. Lett.* **40** \(1978\) 279](#).
- [3] R. Peccei and H. Quinn, *CP conservation in the presence of pseudoparticles*, [*Phys. Rev. Lett.* **38** \(1977\) 1440](#).
- [4] R. Peccei and H. Quinn, *Constraints imposed by CP conservation in the presence of pseudoparticles*, [*Phys. Rev. D* **16** \(1977\) 1791](#).
- [5] J. Preskill, M.B. Wise and F. Wilczek, *Cosmology of the invisible axion*, [*Physics Letters B* **120** \(1983\) 127](#).
- [6] L. Abbott and P. Sikivie, *A cosmological bound on the invisible axion*, [*Physics Letters B* **120** \(1983\) 133](#).
- [7] M. Dine and W. Fischler, *The not-so-harmless axion*, [*Physics Letters B* **120** \(1983\) 137](#).

- [8] H. Primakoff, *Photoproduction of neutral mesons in nuclear electric fields and the mean life of the neutral meson*, *Phys. Rev.* **81** (1951) 899.
- [9] I.G. Irastorza and J. Redondo, *New experimental approaches in the search for axion-like particles*, *Prog. Part. Nucl. Phys.* **102** (2018) 89 [[1801.08127](#)].
- [10] I. Stern, *ADMX Status*, *Proceedings of the Science, 38th International Conference on High Energy Physics ICHEP2016* (2016) 198 [[1612.08296](#)].
- [11] A.K. Yi, S. Ahn, C. Kutlu, J. Kim, B.R. Ko, B.I. Ivanov et al., *Axion Dark Matter Search around $4.55 \mu\text{eV}$ with Dine-Fischler-Srednicki-Zhitnitskii Sensitivity*, *Phys. Rev. Lett.* **130** (2023) 071002.
- [12] CAST collaboration, *New CAST Limit on the Axion-Photon Interaction*, *Nature Phys.* **13** (2017) 584 [[1705.02290](#)].
- [13] E. Armengaud, F.T. Avignone, M. Betz, P. Brax, P. Brun, G. Cantatore et al., *Conceptual design of the International Axion Observatory (IAXO)*, *Journal of Instrumentation* **9** (2014) T05002.
- [14] A. Abeln et al., *Conceptual design of BabyIAXO, the intermediate stage towards the International Axion Observatory*, *Journal of High Energy Physics* **05** (2021) 137.
- [15] S. Ahyoune, A. Álvarez Melcón, S.A. Cuendis, S. Calatroni, C. Cogollos, J. Devlin et al., *A proposal for a low-frequency axion search in the $1\text{--}2 \mu\text{eV}$ range and below with the BabyIAXO magnet*, 2023. [arXiv:2306.17243](#) [physics.ins-det].
- [16] J.M. García-Barceló, A. Álvarez Melcón, A. Díaz-Morcillo, B. Gimeno, A.J. Lozano-Guerrero, J. Monzó-Cabrera et al., *Methods and restrictions to increase the volume of resonant rectangular-section haloscopes for detecting dark matter axions*, *Journal of High Energy Physics* **2023** (2023) 98.
- [17] ADMX collaboration, *Extended Search for the Invisible Axion with the Axion Dark Matter Experiment*, *Phys. Rev. Lett.* **124** (2020) 101303 [[1910.08638](#)].
- [18] HAYSTAC collaboration, *A quantum-enhanced search for dark matter axions*, *Nature Phys.* **590** (2021) 238 [[2008.01853](#)].
- [19] L. Zhong, S. Al Kenany, K.M. Backes, B.M. Brubaker, S.B. Cahn, G. Carosi et al., *Results from phase 1 of the HAYSTAC microwave cavity axion experiment*, *Phys. Rev. D* **97** (2018) 092001.
- [20] A. Álvarez Melcón, S. Argüedas-Cuendis, J. Baier, K. Barth, H. Bräuninger, S. Calatroni et al., *First results of the CAST-RADES haloscope search for axions at $34.67 \mu\text{eV}$* , *J. High Energy Phys.* **2021** (2021) 75 [[2104.13798](#)].
- [21] D. Alesini, D. Babusci, C. Braggio, G. Carugno, N. Crescini, D. D’Agostino et al., *Search for galactic axions with a high- q dielectric cavity*, *Phys. Rev. D* **106** (2022) 052007.
- [22] D. Alesini, D. Babusci, D. Di Gioacchino, C. Gatti, G. Lamanna and C. Ligi, *The KFLASH Proposal*, [1707.06010](#).
- [23] D. Alesini et al., *The future search for low-frequency axions and new physics with the FLASH resonant cavity experiment at Frascati National Laboratories*, [2309.00351](#).
- [24] A. Díaz-Morcillo, J.M. García Barceló, A.J. Lozano Guerrero, P. Navarro, B. Gimeno, S. Argüedas Cuendis et al., *Design of new resonant haloscopes in the search for the dark matter axion: A review of the first steps in the rades collaboration*, *Universe* **8** (2022) .

- [25] B.M. Brubaker, *First results from the HAYSTAC axion search*, 2018.
<https://doi.org/10.48550/arXiv.1801.00835>.
- [26] C.M. Adair et al., *Search for Dark Matter Axions with CAST-CAPP*, *Nature Commun.* **13** (2022) 6180 [[2211.02902](#)].
- [27] B.R. Ko, H. Themann, W. Jang, J. Choi, D. Kim, M.J. Lee et al., *Electric and magnetic energy at axion haloscopes*, *Phys. Rev. D* **94** (2016) 111702.
- [28] J. Choi, H. Themann, M.J. Lee, B.R. Ko and Y.K. Semertzidis, *First axion dark matter search with toroidal geometry*, *Phys. Rev. D* **96** (2017) 061102.
- [29] M. Wooten, A. Droster, A. Kenany, D. Sun, S.M. Lewis and K. van Bibber, *Exploration of wire array metamaterials for the plasma axion haloscope*, *Annalen der Physik* (2023) [2200479](#).
- [30] S. Bae, S. Youn and J. Jeong, *Tunable photonic crystal haloscope for high-mass axion searches*, *Phys. Rev. D* **107** (2023) 015012.
- [31] R.E. Collin, *Foundations for Microwave Engineering*, McGraw-Hill, Inc., second ed. (1992).
- [32] C. Ramella, M. Pirola and S. Corbellini, *Accurate Characterization of High-Q Microwave Resonances for Metrology Applications*, *IEEE Journal of Microwaves* **1** (2021) 610.
- [33] J. Jeong, S. Youn, S. Ahn, C. Kang and Y.K. Semertzidis, *Phase-matching of multiple-cavity detectors for dark matter axion search*, *Astroparticle Physics* **97** (2018) 33.
- [34] S. Arguedas Cuendis et al., *The 3 Cavity Prototypes of RADES: An Axion Detector Using Microwave Filters at CAST*, *Springer Proc. Phys.* **245** (2020) 45 [[1903.04323](#)].
- [35] J.M. García Barceló, A. Álvarez Melcón, S. Arguedas Cuendis, A. Díaz-Morcillo, B. Gimeno, A. Kanareykin et al., *On the development of new tuning and inter-coupling techniques using ferroelectric materials in the detection of dark matter axions*, *IEEE Access* **11** (2023) 30360.
- [36] J. Jeong et al., *Search for Invisible Axion Dark Matter with a Multiple-Cell Haloscope*, *Phys. Rev. Lett.* **125** (2020) 221302 [[2008.10141](#)].
- [37] J. Jeong, S. Youn and J.E. Kim, *Multiple-cell cavity design for high mass axion searches: An extended study*, *Nuclear Instruments and Methods in Physics Research Section A: Accelerators, Spectrometers, Detectors and Associated Equipment* **1053** (2023) 168327.
- [38] A. Álvarez Melcón, S. Arguedas-Cuendis, C. Cogollos, A. Díaz-Morcillo, B. Döbrich, J.D. Gallego et al., *Axion searches with microwave filters: the RADES project*, *Journal of Cosmology and Astroparticle Physics* **040** (2018) 1.
- [39] A. Álvarez Melcón, S. Arguedas-Cuendis, C. Cogollos, A. Díaz-Morcillo, B. Döbrich, J.D. Gallego et al., *Scalable haloscopes for axion dark matter detection in the 30 μ eV range with RADES*, *Journal of High Energy Physics* **084** (2020) 1 .
- [40] L. Zhu, R.R. Mansour and M. Yu, *Compact waveguide dual-band filters and diplexers*, *IEEE Transactions on Microwave Theory and Techniques* **65** (2017) 1525.
- [41] D. Bowring, T. Connolly, M. Kang, M. Ortega, S. Priya, C. Salemi et al., *Dielectric tuning of cavities*, in *3rd Workshop on Cavities and Detectors for Axion Research*, 2018.